coatings

MDPI

Article

Chemical and UV Durability of Hydrophobic and Icephobic Surface Layers on Femtosecond Laser Structured Stainless Steel

Roland Fürbacher *, Gabriel Grünsteidl, Andreas Otto and Gerhard Liedl

Institute of Production Engineering and Photonic Technologies, TU Wien—Vienna University of Technology, Getreidemarkt 9, 1060 Vienna, Austria
* Correspondence: roland.fuerbacher@tuwien.ac.at

Abstract: Femtosecond laser processing significantly alters the surface structure and chemical composition, impacting its wetting properties. Post-treatments such as immersion in a hydrocarbon liquid (petrol) or storage in a vacuum can significantly reduce ice adhesion, making the surfaces interesting for anti-ice applications. This study investigates their durability against acetone, ethylene glycol, and UV radiation. The laser-structured surfaces were immersed in the respective liquids for up to 48 h. The results indicate limited durability of the superhydrophobic and icephobic layers when submerged in acetone and ethylene glycol, with more favorable results for petrol treatment than vacuum treatment. Similar results were obtained after 100 h of UV exposure, showing a decrease in superhydrophobic properties and an increase in ice adhesion. However, repeated vacuum treatments conducted after the chemical durability tests revealed the potential for partial recovery of the hydrophobic and icephobic properties. XPS analysis was performed throughout the experiments to evaluate changes in surface chemistry resulting from the post-laser treatments and the durability tests.

Keywords: surface modification; femtosecond laser processing; nanostructure; microstructure; hydrocarbon treatment; vacuum treatment; chemical durability; superhydrophobic surface; icephobic surface

Citation: Fürbacher, R.; Grünsteidl, G.; Otto, A.; Liedl, G. Chemical and UV Durability of Hydrophobic and Icephobic Surface Layers on Femtosecond Laser Structured Stainless Steel. *Coatings* **2024**, *14*, 924. https://doi.org/10.3390/coatings14080924

Academic Editors: Xiaoming Feng, Bo Li and Hujun Wang

Received: 7 June 2024
Revised: 18 July 2024
Accepted: 20 July 2024
Published: 23 July 2024

1. Introduction

Icephobic surfaces have attracted substantial interest in numerous fields where icing can lead to severe consequences, including wind energy [1–3] and aviation [4,5]. Consequently, modified anti-ice and de-icing surfaces are often exposed to environmental conditions, like wind, dust, and precipitation. In the case of a lift-generating surface, erosion mainly affects the leading edge but can lead to a shortened lifetime and severe damage [6,7]. Within the wind energy sector, leading edge protection (LEP) solutions, such as paint, tapes, and coatings, extend maintenance intervals but usually do not comprise passive ice protection. Nevertheless, wind turbines operated in harsh environments, e.g., offshore or at high altitudes, face a significantly reduced rotor blade lifetime of about two years [6,8] and a reduced annual energy output of 2%–3.7% due to erosion and contamination [7]. In addition, wind turbines exposed to intense icing conditions suffer up to 20% annual electricity production losses [9]. Active anti-icing and de-icing measures, like thermal heating of the affected zones, are energy-consuming and must be precisely controlled to prevent any weakening of the rotor blade's composite structure [10]. Fakorede et al. compared the two primary thermal ice protection systems and found the installation costs of resistive heater sheets to be about 5% of the total costs of a wind turbine, while a hot air injection device is in the range of 1% [11]. During operation, a resistive heater costs 6–12% of the annual energy production compared to 8–14% for the hot air injection. Passive commercial anti-ice surfaces comprise thin polymer films prone to erosion [2,12].

The situation is different for an airplane's wings, where safety regulations require that the leading edge (and other forward-facing parts of the airplane) withstand physical impacts like a bird strike [13]. For this reason, aluminum is the predominant material employed for the leading edge, without any passive anti-icing or de-icing measure. Manufacturers also utilize stainless steel sheets as protective covers, e.g., the horizontal and vertical stabilizers of commercial aircraft like the Airbus A320 [14], or as erosion shields for the rotor blades of helicopters [15,16]. Anti-icing/de-icing is achieved by heating the leading edge via bleed-air from the turbines, electrothermal via heating elements, or other active measures. For ice accretion on the ground, established standards exist specify the proper procedures for aircraft ground-de-icing and the fluids to use (e.g., SAE AS6285 [17]). These de-icing fluids can be categorized as SAE AMS1424 [18] (ISO 11075 [19]) Type I and SAE AMS1428 [20] (ISO 11078 [21]) Type II, III, and IV, and are applied on the aircraft before takeoff, leaving a thin film of fluid on the prepared surfaces. De-icing fluids consist mainly of glycol, which depresses the freezing point of water (FPD), but include surfactants, corrosion inhibitors, thickening agents, defoamers, and other chemicals, which can be ecologically problematic [22]. Therefore, it would be economically and ecologically beneficial if anti- and de-icing could be achieved without extensive heating or the use of chemicals but via passive icephobic surfaces with superhydrophobic properties and low ice adhesion or combined passive/active systems with significantly reduced energy requirements [23,24].

Laser structuring of surfaces is one way to reduce ice accretion in the temperature range around the freezing point by lowering the surface energy and forcing an incomplete wetting state (Cassie–Baxter), which can lead to superhydrophobic properties [25]. Depending on the laser and material properties, such as laser fluence, pulse duration, ablation threshold, and thermal conductivity, different surface structures can be created. If used just below the ablation threshold, short laser pulses can create very small nano-features, otherwise known as laser-induced periodic surface structures (LIPSS). When high pulse energies are applied to a surface, the resulting topography is determined by ablation, remelting, and resolidification processes. Approaches to mathematically model the resulting roughness features after laser processing are based on the segmental cyclic and rhythmic structure of the microrelief [26]. A more accurate model incorporates the amplitude features of the microreliefs to estimate the topography [27].

Sataeva et al. fabricated superhydrophobic surfaces by laser structuring aluminum alloy, subsequently coating the alloy with fluorooxysilane, and performing outdoor tests as well as corrosion tests against NaCl solution, water icing (crystallization-melting cycles), and UV irradiation [28]. The structured samples showed increasing wear and corrosion with increasing test duration. Nevertheless, rough superhydrophobic surfaces do not necessarily offer superior anti-ice or de-icing properties because of the mechanical interlocking with ice [29–31]. Vercillo et al. compared different laser structures to decrease ice adhesion, but used a perfluoropolyether solution in a fluorinated solvent as a coating [32]. A correlation was found between structure roughness and ice adhesion, but the coating's chemical durability or erosion resistance was not determined. In an earlier work, the wettability and ice adhesion of laser-structured steel samples were compared without the use of a coating, and a similar correlation was found: increasing ice adhesion with increasing surface roughness [33]. Through the application of LIPSS, the static water contact angle was increased without further increasing the ice adhesion shear stress.

Considering these findings, laser-structured surfaces could fulfill both industry sectors' requirements if they prove to have equal passive anti-ice and de-icing properties combined with a high erosion/chemical resistance. In an earlier work, superhydrophobic stainless steel surfaces were produced via femtosecond laser processing and subsequent hydrocarbon treatment, leading to superhydrophobicity and a significant reduction in ice adhesion of 57% [34]. The resulting ice adhesion correlated with the structure roughness, where shallow LIPSS showed the lowest ice adhesion in the range of 250 kPa. Further application-oriented experiments in a small-scale icing wind tunnel showed a considerable delay in the icing of a laser-structured and hydrocarbon-treated sample attached to an airfoil segment [35]. The resulting ice shape was smoother along the leading edge, with a high probability of being aerodynamically beneficial. Fürbacher et al. demonstrated the erosion resistance of micro- and nanostructures during a long-term field test on a small-scale wind turbine under alpine operating conditions. Therefore, laser-structured stainless steel foils were attached to the leading edges of the rotor blades and showed only minor erosion after six winter months of operation.

At the time of this publication, direct laser structuring was limited to smaller surface areas due to the relatively long processing times. Nevertheless, the transfer of microstructures to metal and plastic surfaces using embossing processes offers an economically relevant option for large-area applications and has already been successfully implemented [36–38]. When using laser-structured steel tools, microstructures can be transferred very well to PET and PMMA substrates, significantly improving the wetting behavior [39]. Studies on PTFE films have led to significantly reduced ice adhesion after imprinting a laser-generated structure [40].

The work of different scientific groups indicates that the contact angle hysteresis (CAH), in combination with the static contact angle (SCA), plays a vital role in describing the icing behavior of superhydrophobic surfaces, and therefore, their ice-repellent properties [41,42]. Janjua et al. recommend a small CAH in addition to high SCA to produce surfaces with icephobic properties and potentially reduce runback ice accretion on aircraft wings and wind turbine rotor blades [43]. However, contrasting findings by Momen et al. have demonstrated that ice adhesion strength is not a direct function of CAH. Therefore, the CAH does not directly correlate with the icephobic properties [44]. Through a modified Cassie–Baxter relation, the CAH can predict the roll-off angle (RoA) of textured surfaces [45]. Therefore, the SCA, CAH, and ice adhesion were compared in this work to understand their correlation better. Previous investigations on femtosecond laser surface processing were expanded, and the chemical resistance of superhydrophobic and icephobic surface layers formed during our novel hydrocarbon treatment was examined. Hydrocarbon and vacuum treatments were compared in this study, as well as the influence of the initial laser-generated structure type and size on the wettability and anti-ice/de-icing performance. Chemical durability tests were conducted to demonstrate the potential for industrial applications. During these tests, the samples were immersed in an acetone and ethylene glycol bath. These liquids were chosen because acetone is an organic solvent with excellent solubility for the carbon compounds responsible for the wettability transformation and reduced ice adhesion [46]. As mentioned before, ethylene glycol solutions are used as chemical de-icing fluids and are of significant interest to the aviation sector. A UV-radiation test was conducted, which is part of the standard procedure for testing the durability of coatings for sunlight-exposed applications like outer aircraft components or wind turbine rotor blades.

2. Materials and Methods

2.1. Material

Cold-rolled stainless steel (1.4301/AISI 304) with a thickness of 2 mm was used as the substrate material for the experiments. Before undergoing laser processing, the substrates were cleaned with acetone and air-dried.

2.2. Laser Processing

The samples were structured using a femtosecond laser system Femtopower Compact Pro (Spectra-Physics, Vienna, Austria) consisting of a Ti:Sapphire oscillator and a multi-pass Ti:Sapphire amplifier, which emits broadband 30 fs laser pulses at a rate of 1 kHz (Figure 1). Laser pulses can carry a maximum pulse energy of 0.8 mJ at 800 nm central wavelength and a bandwidth of 40 nm. Due to its internal setup, the output radiation is linearly polarized, which is required to form a channel-like LIPSS. A variable attenuator was used to adjust the laser fluence on the specimens' surface. The laser beam was focused by a plano-convex spherical lens with a focal length of 80 mm. During all experiments, a Gaussian intensity distribution was used. Based on previous experiments [34], the same four different laser structure types were selected for further testing. LIPSS were generated off-focus by overlapping linear tracks, and grid and triangle structures were created by intersecting tracks at 90° or 60°, respectively. Micro-dimple arrays were generated by repetitive static laser ablation.

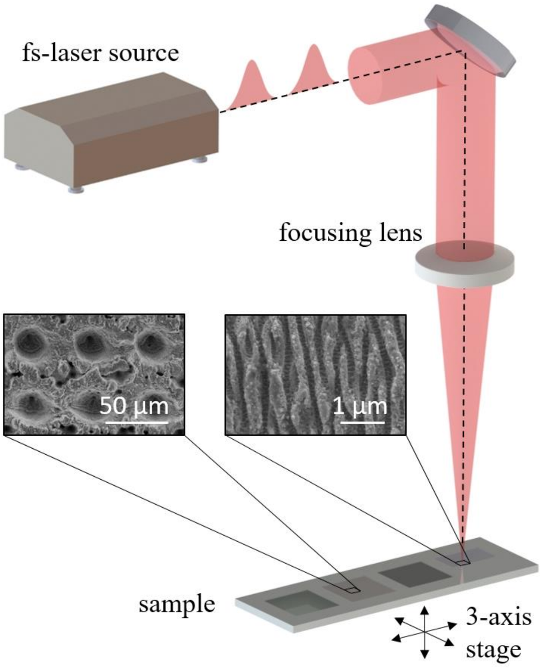

Figure 1. Schematic depiction of the femtosecond laser machining setup.

On each sample, four different surface structures (LIPSS, grid, dimple, and triangle) were applied with laser parameters according to Table 1 and the resulting roughness properties according to Table 2. As a reference, one sample was stored under ambient air conditions after laser processing (C#Ref).

Table 1. Laser machining parameters of the tested samples.

Structure Type	Laser Fluence [J/cm^2]	Spot Diameter [µm]	Hatch Distance [µm]	Number of Laser Pulses Per Area
LIPSS	1	150	150	15
Grid	30	35	100	18
Dimple	40	35	50	40
Triangle	20	35	100	18

Table 2. Surface topography after laser processing, before testing; λc—roughness cut-off wavelength, Sa—arithmetic mean deviation, Sq—root mean square height, Sz—maximum height, Sdr—developed interfacial area ratio.

Structure Type	λc [nm]	Sa [µm]	Sq [µm]	Sz [µm]	Sdr [%]
LIPSS	75	0.1	0.2	4.0	0.5
Grid	150	4.7	6.2	41.0	203
Dimple	300	16.2	18.3	77.7	1235
Triangle	150	3.6	4.7	32.9	116

2.3. Surface Characterization

The geometric surface properties of the laser-processed samples were obtained using a Bruker Alicona Infinite Focus 3D surface measurement system, which uses the method of focus variation to retrieve surface topography information. A Jeol JCM-5000 instrument (Jeol, Akishima, Japan) was used for SEM imaging.

2.4. Wettability Acceleration Treatment

Immediately after femtosecond laser processing, metal surfaces tend to be superhydrophilic and evolve to a hydrophobic state over several days to weeks when stored in ambient air [47,48]. The samples were placed in a vacuum chamber or immersed in Eurosuper petrol (RON 95) inside a sealed HDPE barrel to accelerate the wetting transformation time. The duration of the treatment was set to 4 h (one cycle) based on our previous work, in which the focus was on the wetting transformation time of laser-structured samples stored in different media [34]. The same SEM instrument (Jeol JCM-5000) was used for the imaging and vacuum treatment; however, the electron beam was turned off during the latter. Its turbomolecular pump provided a pressure of less than 10^{-4} mbar in the specimen chamber.

X-ray photoelectron spectroscopy (XPS) was performed to identify the changes in surface chemistry. A SPECS XP-spectrometer equipped with a monochromatic Al-Kα X-ray source (µFocus 350) and a hemispherical WAL-150 analyzer with an acceptance angle of 60° was used. Pass energies of 100 eV and 30 eV and step widths of 0.5 eV and 50 meV were used for survey and detail spectra, respectively (excitation energy: 1486.6 eV, beam energy and spot size: 100 W onto 400 µm; mean angle: 51° to sample surface normal; base pressure: 2×10^{-9} mbar, pressure during measurements: $<5 \times 10^{-9}$ mbar). The analysis depth was typically around 7–10 nm. Data analysis was performed using CASA XPS software (version 2.3.25PR1.0), employing Shirley backgrounds and Scofield sensitivity factors. No charge correction was applied. Deconvolution of the spectra was carried out using Gaussian-Lorentzian peaks (GL(30)) if not stated otherwise.

2.5. Wettability Properties and De-Icing

A DataPhysics contact angle goniometer OCA25 with a 0.4 mm blunt tip cannula was used to evaluate the wettability properties of the laser-treated samples. The sessile drop method with a polynomial fitting was applied to obtain the static contact angles (SCA) utilizing a water drop volume of 10 µL. For the advancing (ACA) and receding contact angles (RCA), the needle-in method with elliptical fitting was applied. The ACA and RCA measurements were started with an initial drop volume of 5 µL, increased the volume to 100 µL at a rate of 10 µL/s, reduced the volume again to the initial value after a delay time of 2 s, and repeated each measurement twice. The water volume needed for an adequate advancing and receding contact angle measurement (ARCA) was estimated based on the approximations proposed by Korhonen et al. [49]. Furthermore, the contact angle hysteresis (CAH) was calculated as the difference between the ACA and RCA.

The ice adhesion shear stress at the interface was measured using the cuvette-encased ice column method, a process similar to the setup described by Meuler et al. (Figure 2) [50]. In this setup, disposable cuvettes (polystyrene) were placed open-side down on the laser-structured surface, which was then cooled for 15 min to a temperature of −30 °C by a Peltier cooling element (TC160Pro, DataPhysics, Filderstadt, Germany). The temperature was measured between the cooling element and the sample. After 15 min, 1 mL of distilled water was injected through a hole in the cuvette using a syringe and an automated dispenser at a rate of 170 µL/s. After a freezing time of 15 min, the ice column was sheared off by a stepper motor (103H7123, Sanyo Denki, Moriguchi, Japan) driven force probe (3 mm above the sample surface) connected to a force transducer (Typ S2 500N with an AE301 interface, Hottinger Baldwin Messtechnik HBM, Darmstadt, Germany). The analog voltage signal was recorded using an interface (NI USB-6009, Texas Instruments, Dallas, TX, USA) and LabView 2023 software. The ice adhesion shear stress was calculated by dividing the measured force by the interface area of 10 mm × 10 mm, although it is essential to note that there is a mixed shear/tensile mode due to the height of the push-force application point [51]. Since all measurements were performed under the same conditions, the effect of the push height was not covered in this work. For laser-structured stainless steel, a few cycles of ice adhesion measurements do not affect the structure's micro-geometry or surface roughness [33].

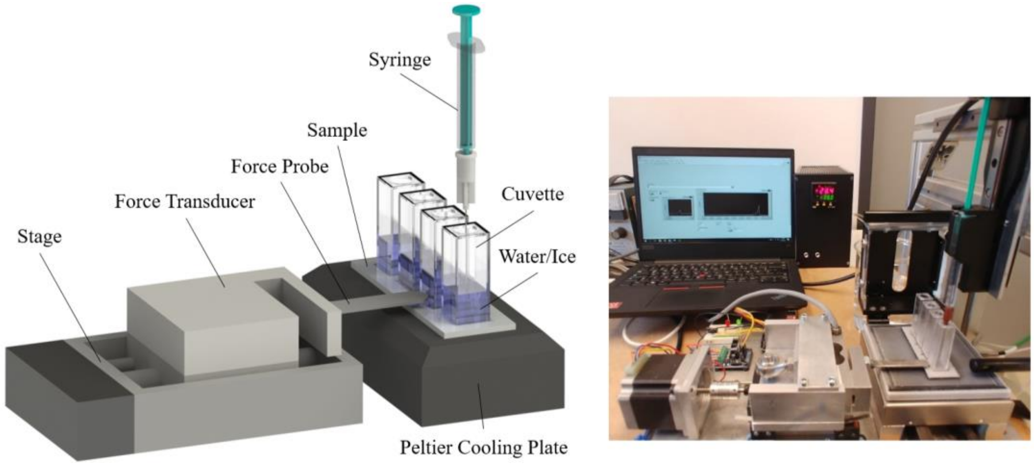

Figure 2. Schematic depiction of the ice adhesion test rig (**left**) and actual setup with an open cover (**right**).

2.6. Chemical Durability

After femtosecond laser processing and chemical treatment, the hydrophobic surfaces were tested for their chemical resistance against acetone and a standard de-icing fluid solution. Acetone (purity > 99.9%) was chosen because it is an organic solvent, which is supposed to represent a challenge to the hydrocarbon layers applied during chemical post-laser treatment. Furthermore, in the literature, the chemical resilience of superhydrophobic surfaces was also tested against acetone and other organic solvents. Yang et al. produced superhydrophobic surfaces on carbon fiber-reinforced polymer composites by picosecond laser direct writing, dip coated with fluoroalkylsilane (FAS), and were able to achieve SCAs of 155° [46]. After 1 h of immersion in acetone, the surfaces were again measured, and SCAs > 150° were observed. Therefore, good resistance against aqueous solutions was assumed. No more measurements after the initial 1 h were carried out.

Since robust, icephobic surfaces are of significant interest to the aerospace industry, a commonly used de-icing agent for aircraft ground de-icing was chosen as a second liquid, consisting mainly of glycol alcohols [52]. This glycol solution corresponds to the conventional ISO/SAE Type I air de-icing fluid and was mixed with 85% ethylene glycol and 15% water. According to SAE AS6285 C and the FAA holdover time guidelines (2023–2024), the holdover time for SAE Type I fluid varies from 2 min under freezing rain conditions to 45 min under active frost conditions [53]. During this period, the aircraft must take off—if not, the de-icing and anti-icing procedures must be repeated.

To test the chemical resistance, the samples were then immersed in an acetone or glycol solution for 48 h. After predefined time intervals, the samples were removed from the chemicals and tested for SCA, ice adhesion, and CAH. Contact angle and ice adhesion measurements were conducted for each sample after total immersion times of 1, 4, 24, and 48 h. After each liquid extraction, the samples were dried again with filtered compressed air at 5 bar. The results shown in Section 3 are the average values of multiple measurements. The measured values and standard deviations can be found in the Supplementary Material (Table S1). Thus, statements could be made about the wetting and ice-repellent properties of the produced surfaces via the SCA, CAH, and ice adhesion measurements.

2.7. Optical Durability Setup (UV)

To simulate environmental exposure to sunlight, the laser-structured and hydrocarbon/vacuum-treated samples were irradiated by a Xenon arc source with a daylight filter (ASTM D7869 [54]). The test conditions were in accordance with IEC TS 62788-7-2 [55], using an irradiance of 0.8 $W/m^2/nm$ at 340 nm wavelength, equivalent to 81 ± 8 W/m^2. Inside the test chamber, air was maintained at a temperature of 65 ± 3 °C and a relative humidity of 20 ± 5%.

3. Results and Discussion

3.1. Surface Structures

Figure 3 shows the four structure types tested in the following experiments:

- Nanostructures (type 1)—LIPSS: This structure can be described as parallel channels with a sine-wave-like cross-section, a depth of several 10–100 nm, and a spatial period tied to the wavelength of the laser light used to create it [56–58]. A FFT of SEM micrographs was used to determine the spatial frequency of the LIPSS. Our case resulted in a mean spatial period of 560 nm, consistent with previous findings for this laser/material combination [59]. Further analysis of these structures using atomic force microscopy (FEI Quanta 250 FEG + GeTEC AFSEM) revealed a vertical depth of 300 nm.
- Microstructures (types 2, 3, and 4)—grid, dimple, and triangle: In contrast to LIPSS, three different microstructures were applied with a laser fluence in the ablation regime of the substrate material. Because of the Gaussian intensity distribution and linear polarization of the used laser beam, the created microstructures are superimposed by LIPSS nanostructures and can be regarded as hierarchical structures. By creating a rough surface, attempts were made to favor the Cassie–Baxter wetting mode, in which vapor is "trapped" under the water fraction in the interface, over the Wenzel wetting mode, in which the entire surface under the liquid is wetted, thereby increasing hydrophobicity [60].

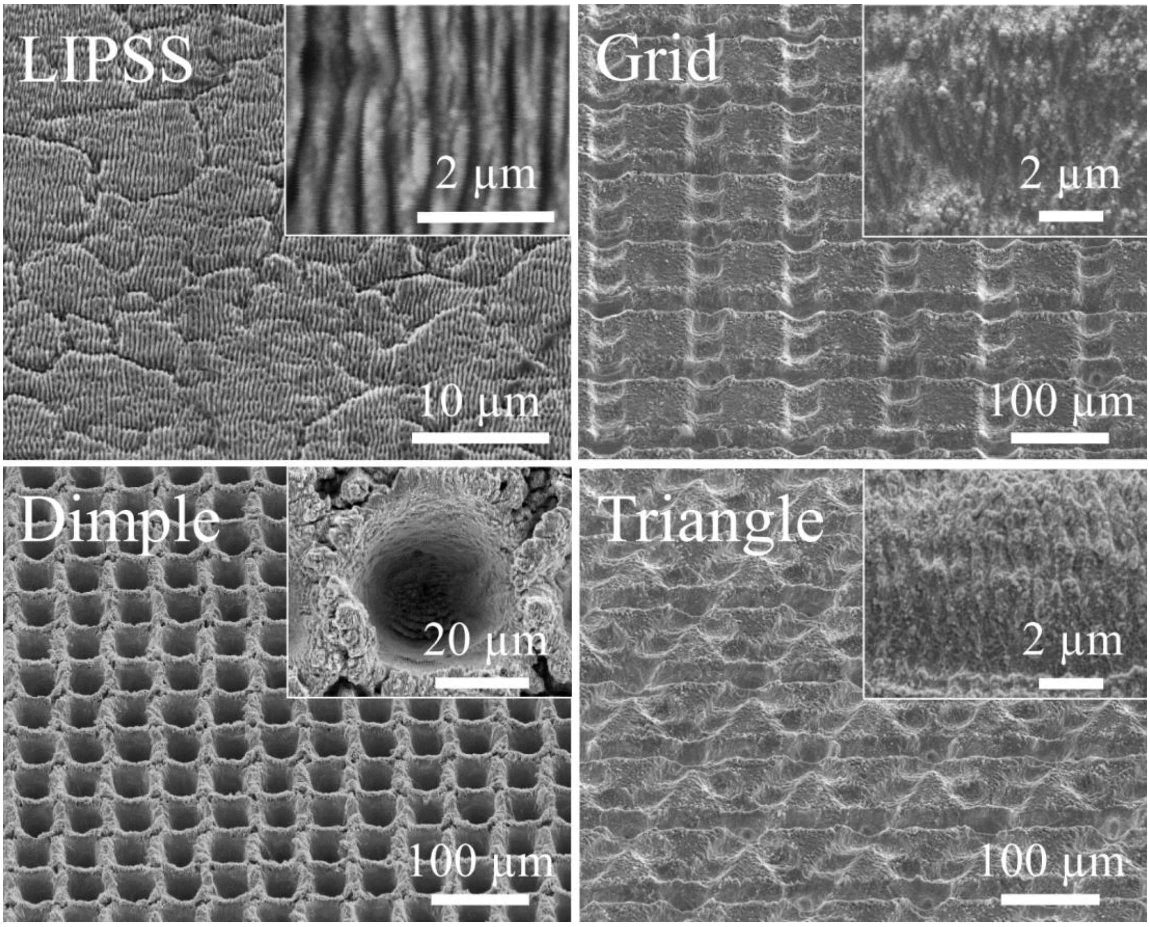

Figure 3. SEM images: laser structures taken at a 45° tilt angle (close-ups have been taken without tilt). LIPSS nanostructure with a spatial period of 560 µm. Grid, dimple, and triangle microstructures feature superimposed LIPSS nanostructures.

3.2. Acetone Durability

After applying the previously described vacuum treatment to the femtosecond laser-processed surfaces, an average SCA of 161° for all samples was measured (Figure 4). Similarly, the petrol-treated samples exhibited good superhydrophobic wettability, with an average SCA of 157°. Notably, the dimple structures showed the highest SCAs for both treatment methods, with an average of 164°. Subsequently, the chemical resistance against acetone of the vacuum- and petrol-treated superhydrophobic surfaces is presented below for immersion times of 1, 4, 24, and 48 h. After 1 h in acetone, the superhydrophobic properties of our petrol-treated samples were maintained, with an average SCA of 157° (Figure 4). While showing a slight deterioration compared to the petrol-treated samples, the vacuum-treated samples still displayed nearly superhydrophobic wettability, with an average SCA of 150°. However, after 4 h, the SCA decreased significantly, and after 24 h, the surfaces became hydrophilic, reaching their minimum SCA. In contrast, the petrol-treated samples exhibited a high SCA after 48 h (108°–153°), depending on the surface structure, and, therefore, continued to be hydrophobic after 48 h. Among the different surface structures, the dimple structure of the petrol-treated sample showed the best result, with an SCA of 153° after the overall immersion time.

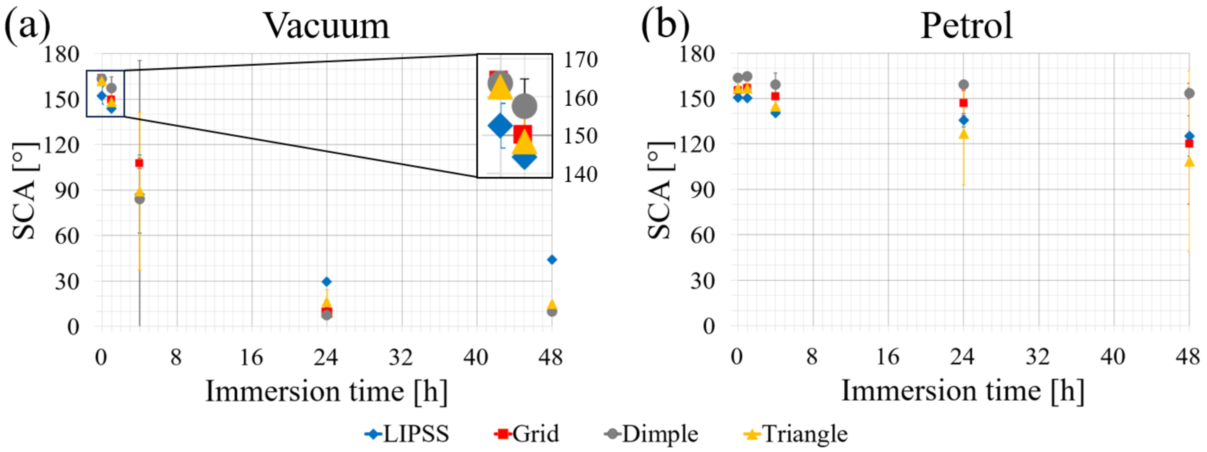

Figure 4. Plot of the static contact angle (SCA) over the immersion time in acetone for (**a**) vacuum-treated samples and (**b**) petrol-treated samples with different structure types.

The measured ice adhesion for the untreated stainless steel samples showed an average of 820 kPa. All superhydrophobic surfaces achieved better de-icing results, except for the vacuum-treated dimple structures (Figure 5). Despite the dimple structures initially having the best hydrophobic properties, the ice adhesion values were significantly worse in comparison to those of all the other structures. This discrepancy can be attributed to the crucial role of the surface roughness and the depth of the structure at the ice-to-surface interface, as highlighted by Vercillo et al. [32]. Since the dimple structure is the roughest among all the compared structures (Table 2), the Cassie–Baxter wetting state could not be achieved completely, resulting in interlocking between the ice and the sample, leading to high ice adhesion shear stresses. The lowest adhesion was achieved for the vacuum-treated LIPSS surface with only 95 kPa. This represents a decrease of 88% compared to the untreated stainless steel sample. The grid and triangle structures obtained the lowest initial adhesion of 364 kPa among the petrol-treated samples.

Examination of the chemical durability tests indicated that after 1 h of immersion time in acetone, the ice adhesion shear stresses increased significantly in comparison to the initial values for the vacuum-treated samples (Figure 5). In contrast, the petrol-treated samples nearly maintained their initial values even after 1 h of immersion in acetone (LIPSS, grid, and triangle structure). However, the maximum values were reached after 4 h for the vacuum-treated samples (average adhesion of 983 kPa) and after 48 h for the petrol-treated samples (average adhesion of 875 kPa).

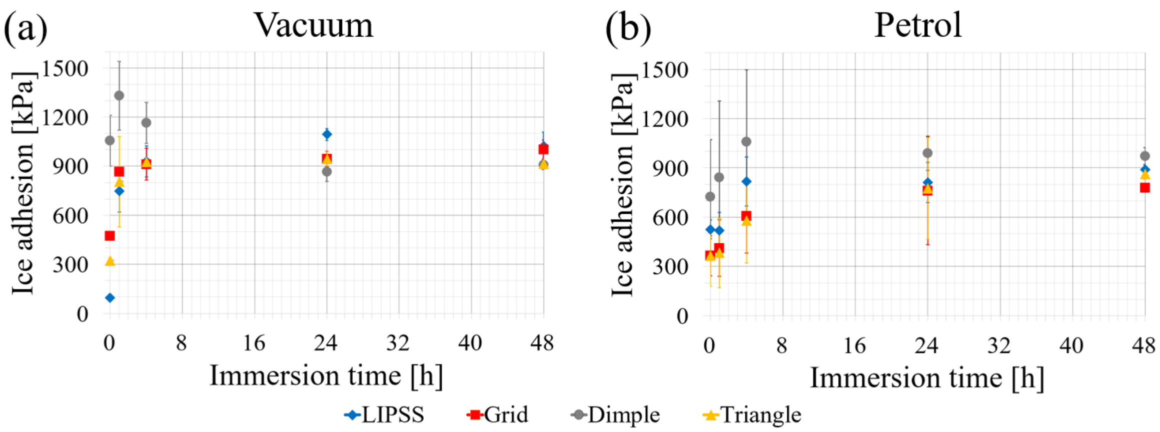

Figure 5. Plot of the ice adhesion over the immersion time in acetone for (**a**) vacuum-treated samples and (**b**) petrol-treated samples with different structure types.

During the chemical durability tests, the CAH and RoA underwent significant changes with increasing immersion time in the chemicals. When the water droplet no longer rolls off the tested surface, making RoA measurements impractical, the CAH becomes more suitable for characterizing the wetting behavior, especially in the transition phase from hydrophobic to hydrophilic.

The grid, dimples, and triangle structures of the vacuum-treated samples exhibited a low average initial CAH of 38° (Figure 6). Interestingly, the CAH of LIPSS, which showed the lowest initial ice adhesion of all the structures tested, resulted in an average of 72°. Additionally, for the petrol-treated samples, the dimple structure, which previously exhibited the strongest ice adhesion shear stresses, showed clearly the lowest average CAH of 11°. Both of these findings support Momen et al.'s assumption that the CAH does not linearly correlate with ice adhesion [44]. A further CAH evaluation revealed a strong, substantial increase in the CAHs after 1 h for the vacuum-treated samples and only slight changes for the petrol-treated samples (Figure 6). Subsequently, after 4 h, a sharp CAH decrease in the vacuum-treated samples occurred due to the transition from the hydrophobic to the hydrophilic wettability regime. In contrast, the petrol-treated samples displayed a different behavior. Here, on average, only a slight deviation of the CAH occurred after 1 h; however, after 4 h, the CAHs increased clearly for the grid, dimple, and triangle structures. Overall, the petrol-treated surfaces remained hydrophobic throughout the experiment.

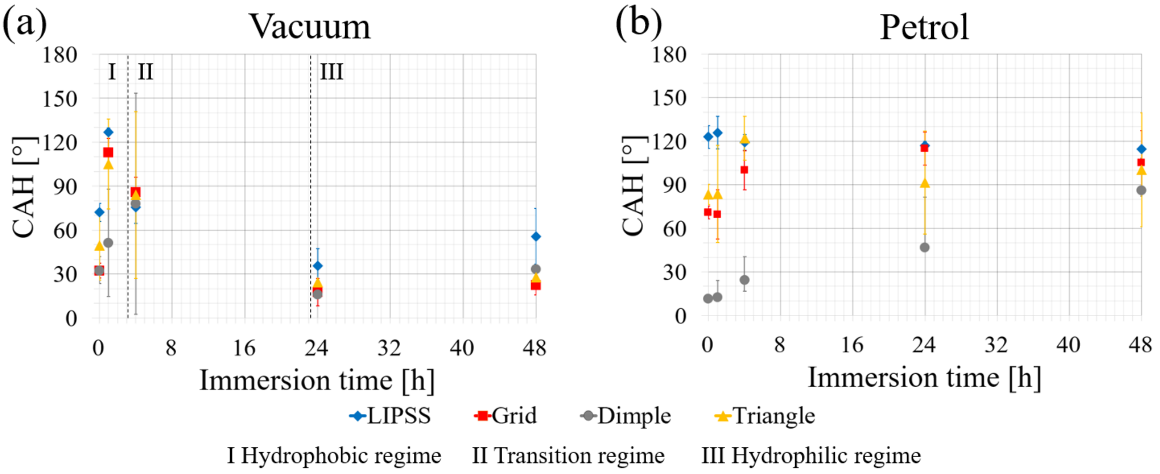

Figure 6. Plot of the contact angle hysteresis (CAH) over the immersion time in acetone for (**a**) vacuum-treated samples and (**b**) petrol-treated samples with different structure types.

3.3. Ethylene Glycol Solution Durability

The results of the chemical durability tests with de-icing fluid showed that for both treatment methods, the high SCAs and the hydrophobic properties were preserved after 1 h of immersion (Figure 7) (average SCA of vacuum-treated samples after 1 h: 153°; average SCA of the petrol-treated sample after 1 h: 153°). However, for the vacuum-treated samples, the SCA dropped significantly after 4 h, and after 24 h, a minimum was reached (average SCA: 42°). A similar behavior has already been observed in previous tests with acetone, although the average minimum SCA for the vacuum-treated samples was higher for glycol (42°) than for acetone (16°). For the samples treated with petrol, hydrophobic wettability was maintained (average SCA of 139°) even after 48 h and remained within the threshold of superhydrophobicity. Again, the value of the average SCA after 48 h exceeded that measured during the acetone resistance tests. Among the different structure types, the grid structure exhibited the best results after the overall immersion time in the glycol solution, with an average SCA of 146°.

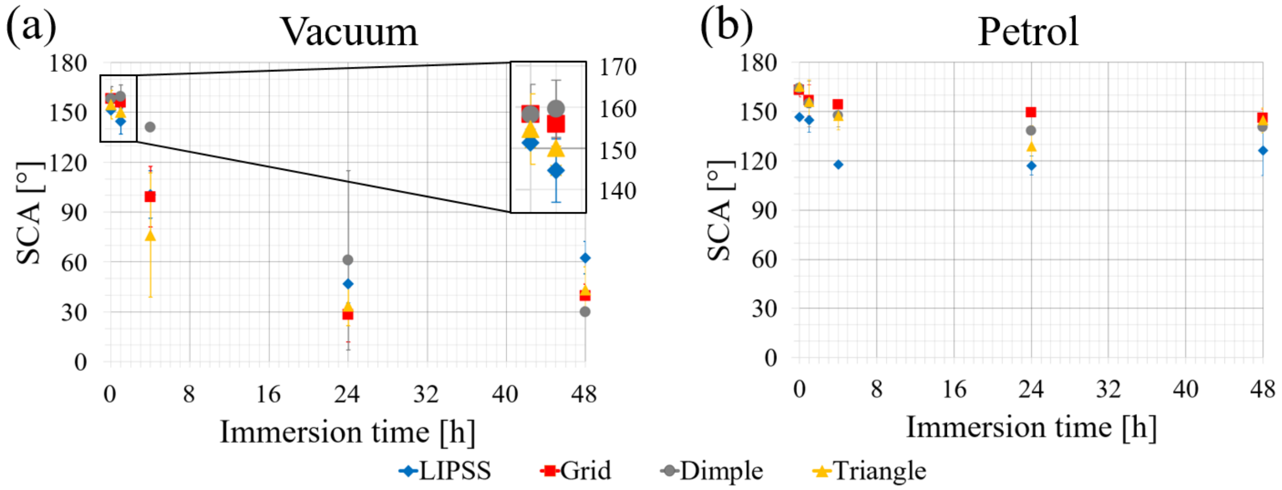

Figure 7. Plot of the static contact angle (SCA) over the immersion time in ethylene glycol solution for (**a**) vacuum-treated samples and (**b**) petrol-treated samples with different structure types.

The best de-icing properties were achieved with vacuum-treated LIPSS, which had an ice adhesion of 115 kPa, while the grid structure exhibited the most favorable results for the petrol-treated sample at 340 kPa. Additionally, as explained beforehand, the dimple structure showed the highest initial adhesion shear stress of 1176 kPa compared to the other surfaces and the untreated and unstructured stainless steel sample (820 kPa).

The ice adhesion measurements displayed an increase for both treatment methods after just 1 h of immersion time, with the maximum levels being reached after 24 h (Figure 8). The petrol-treated samples outperformed the vacuum-treated samples (average adhesion of petrol-treated samples without dimple structures: 790 kPa; average adhesion of vacuum-treated samples: 911 kPa).

Due to the mechanical interlocking between ice and rough surface [30], dimple structures showed a significant increase in ice adhesion for both treatment methods compared to the other structure types. However, as observed previously in the acetone resistance test, the CAH of the dimple structures resulted in a low initial CAH (average CAH vacuum-treated dimple structure: 25°; average CAH petrol-treated dimple structure: 9°). Furthermore, the best de-icing properties were achieved with vacuum-treated LIPSS structures, which also showed the highest initial average CAH (92°). These results further support the findings and assumptions of Momen et al. [44].

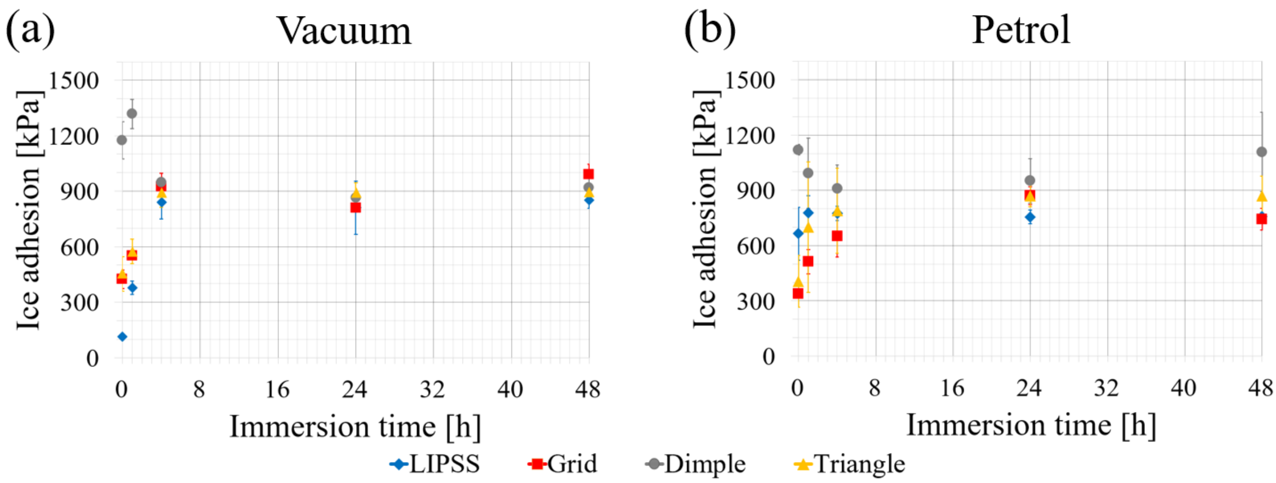

Figure 8. Plot of the ice adhesion over the immersion time in an ethylene glycol solution for (**a**) vacuum-treated samples and (**b**) petrol-treated samples with different structure types.

Similar to the behavior observed with acetone, the CAH increased after 1 h of immersion for the vacuum-treated samples (Figure 9), reaching a maximum after 1 h (LIPSS), and 4 h (grid, dimple, and triangle). After that, the CAH decreased significantly after 24 h. The petrol-treated samples showed a continuous CAH increase until 24 h of immersion time (except for the LIPSS structures) and remained in their initial hydrophobic state. For both treatment methods, an unexpected gradient change occurred after a test duration of 48-h compared to the results after 24 h. Obviously, after the durability tests, the laser-structured surfaces remain susceptible to the chemisorption of airborne hydrocarbons, which results in a renewed conversion of the chemical polarity from polar to non-polar, and, therefore, to hydrophobic wettability [61]. Since the samples were stored in ambient air for a few days between the sample extraction from the ethylene glycol solution and the 48 h measurement, the beginning of this transformation process can be assumed. The slight increase in the SCA (for LIPSS, Grid, Triangle) and the gradient change of the CAH after 48 h support this hypothesis. Based on these observations, the question arose as to what extent the structures could regenerate their hydrophobic and de-icing capabilities after the durability tests.

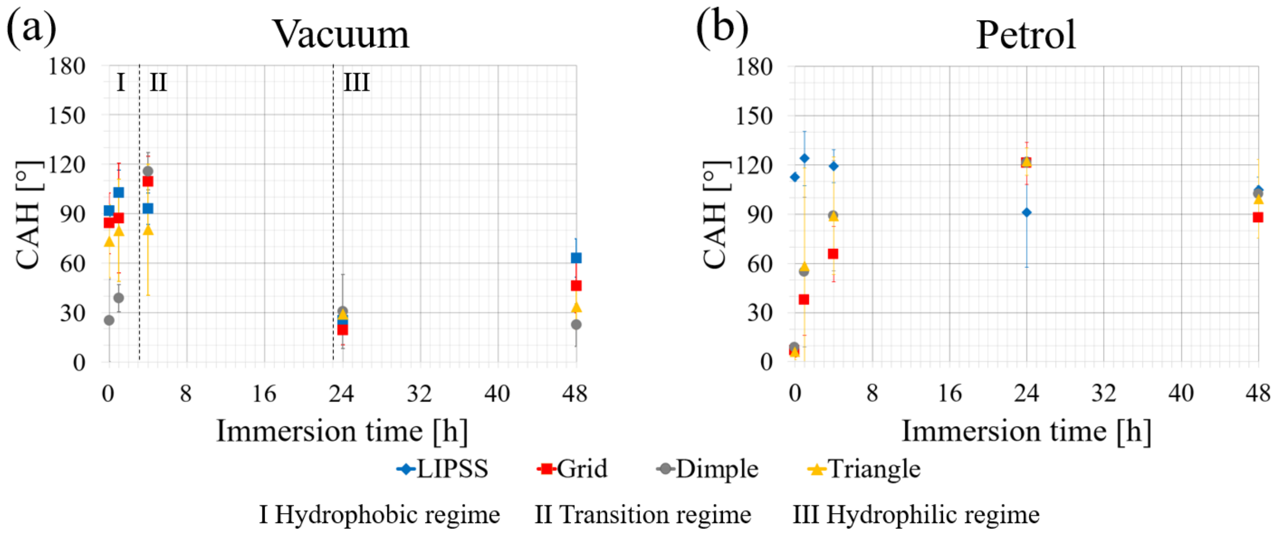

Figure 9. Plot of the contact angle hysteresis (CAH) over the immersion time in ethylene glycol solution for (**a**) vacuum-treated samples and (**b**) petrol-treated samples with different structure types.

To investigate the potential regenerative capabilities of the examined surfaces and recover the hydro- and icephobic properties after testing, the vacuum-treated samples were again exposed to the corresponding treatment method for 4 h. Overall, after the second treatment cycle, the results of the SCA measurements indicated a recovery of the superhydrophobic wettability (Table 3). However, a slight decrease in SCA and ice adhesion was observed, which may be further improved by extending the treatment duration.

Table 3. Regenerative capability of vacuum-treated samples after 48 h of acetone immersion and repeated vacuum treatment for 4 h; IA—ice adhesion, vac.—vacuum treatment.

Sample ID	Structure Type	Treatment Method	Initial SCA [°]	SCA 48 h [°]	SCA 48 h + 4 h vac. [°]	Initial IA [kPa]	IA 48 h [kPa]	IA 48 h + 4 h vac. [kPa]
C#1	LIPSS	Vacuum	148	42	148	102	1084	567
	Grid		164	12	153	469	1042	678
	Dimple		164	10	151	947	926	1359
	Triangle		162	15	149	310	914	687

Overall, it was shown that petrol-treated samples could maintain hydrophobic wettability even after 48 h of immersion in acetone and ethylene glycol solution and, therefore, exhibited acceptable chemical resistance in terms of SCA and hydrophobic properties. The vacuum-treated samples maintained their initial hydrophobicity for 1 h, after which a significant deterioration occurred. Regarding ice adhesion, petrol-treated samples outperformed vacuum-treated samples. However, the icephobic properties could not be maintained. Depending on the liquid, a decrease occurred at 1 h (glycol solution) and 4 h (acetone). A rapid increase in ice adhesion was observed for the vacuum-treated samples. Both sample treatments did, therefore, not provide satisfying resistance in terms of the de-icing capabilities. Notably, the petrol treatment showed better resistance to the glycol solution than to acetone. Furthermore, it was demonstrated that re-exposure to a vacuum after acetone immersion can recover the hydrophobic wettability of these surfaces and partially recover the de-icing performance. Moreover, the measurements indicated that the CAH does not directly correlate to the ice adhesion.

3.4. XPS Analysis

Since our previous research has demonstrated that the transition of femtosecond processed surfaces from hydrophilic to superhydrophobic wettability occurs faster and more effectively when treated with Eurosuper petrol RON 95 in comparison to Petroleum benzine 60–95, it is to be assumed that the fuel additives play a crucial role in the transformation of the surface structures [22]. Furthermore, the distinct immersion time-dependent differences between the above-described vacuum and petrol-treated samples may also be attributable to these additives. For this reason, a detailed investigation of the surface chemical compounds is of great interest to understand the underlying processes. However, the lack of manufacturer information on fuel additive ingredients complicates the accurate analysis of chemical compounds. Nevertheless, a comprehensive XPS analysis was performed, but only data on the chemical groups and their polarity could be collected due to its limitations.

As expected, the survey spectra showed the presence of the major elements C, O, and Fe. The laser structuring process leads to an increase in oxygen levels, regardless of the structure type. The increase in oxygen levels could be attributed to the formation of oxides resulting from the melting of the material. During the laser process, carbon contamination on the surface was removed, which resulted in a significant drop in carbon content. The experimental results showed a strong correlation between the chemical treatments and the surfaces' iron-to-carbon ratio, which was, on average, reduced by 76% after vacuum treatment (C#RefVac) and by 69% after petrol treatment (C#RefPet) (Table 4). The increase in carbon can be explained by the formation of a new surface layer, which is created by the chemisorption of hydrocarbons [62]. This effect was structure-dependent and favored dimple, grid, and LIPSS structures over the triangle structure. This dependence is likely related to the applied accumulated laser fluence, which was valid for dimple and grid structures but not LIPSS (Table 5).

Table 4. Results of the XPS measurements; survey spectra: Fe/C change when compared to the respective structure of the untreated reference sample; detail spectra: non-polar and polar component ratio change after vacuum/hydrocarbon treatment and durability tests; SCA and ice adhesion as performance indicators.

Sample ID	Structure Type	Survey	C1s		Performance	
		Fe/C Change to C#Ref [%]	**NP/P Change to Storage in Ambient Air (C#Ref) [%]**	**Mean NP/P Change [%]**	**SCA [°]**	**Ice Adhesion [kPa]**
C#1 Vacuum treated, Acetone immersion	LIPSS	−62	16	24	44	1022
	Grid	−59	18		10	1001
	Dimple	−58	36		10	906
	Triangle	−2	35		15	914
C#2 Petrol treated, Acetone immersion	LIPSS	−83	96	88	125	888
	Grid	−50	69		120	777
	Dimple	−74	138		153	972
	Triangle	−10	54		109	862
C#3 Vacuum treated, Ethylene glycol immersion	LIPSS	−65	41	32	63	852
	Grid	−13	43		40	989
	Dimple	−40	52		30	917
	Triangle	33	−8		43	893
C#4 Petrol treated, Ethylene glycol immersion	LIPSS	−77	42	44	126	758
	Grid	−58	28		146	744
	Dimple	−64	52		141	1108
	Triangle	−34	53		145	868
C#RefVac, Vacuum treated	LIPSS	−80	129	190	152	172
	Grid	−74	174		152	526
	Dimple	−81	219		160	1193
	Triangle	−68	276		153	330
C#RefPet, Petrol treated	LIPSS	−72	110	187	150	680
	Grid	−72	232		166	328
	Dimple	−78	248		164	1027
	Triangle	−52	220		163	282
C#Ref untreated	LIPSS				66/133 *	805 **
	Grid				0/26 *	951 **
	Dimple				0/106 *	902 **
	Triangle				0/21 *	861 **
	Reference				69	821

* SCA measured after 21/218 days of ambient air exposure. ** Ice adhesion measured after 14 days of ambient air exposure.

Table 5. Laser machining parameters of the tested samples and Fe/C change due to laser processing and chemical treatment (vacuum/petrol), sorted by accumulated laser fluence.

Sample ID	Structure Type	Laser Fluence [J/cm^2]	Accumulated Laser Fluence [J/cm^2]	Fe/C Change to C#Ref [%]
C#RefVac	Dimple	40	815	−81
C#RefPet	Dimple	40	815	−78
C#RefVac	Grid	30	382	−74
C#RefPet	Grid	30	382	−72
C#RefVac	Triangle	20	382	−68
C#RefPet	Triangle	20	382	−52
C#RefVac	LIPSS	1	17	−80
C#RefPet	LIPSS	1	17	−72

Combined with the surface topography, the amount of non-polar components on the surface determines its wettability. The investigation was therefore focused on the ratio between non-polar (NP) components (C-C/C-H) and polar (P) components (C-OH/C-O-C, C=O, O-C=O). The C1s detailed spectra of the vacuum (C#RefVac)-and petrol (C#RefPet)-treated samples revealed a 185% increase in non-polar C-C/C-H components, which led to hydrophobization of the surfaces (Figure 10c,d). After the immersion of samples C#1 and C#2 in acetone for 48 h, the Fe/C ratio increased significantly, but the mean reduction was still 45% (C#1) and 54% (C#2). This average includes the triangle structures that did not experience the same transition (Table 4). By excluding the triangle structure, the average reduction in the Fe/C ratio after acetone immersion was 60% after vacuum treatment and 69% after petrol treatment. With reduced ratios of 62% (C#1) and 83% (C#2), LIPSS showed the highest resistance regarding the total carbon left on the surface, but primarily polar components, which are hydrophilic. After acetone immersion, the C1s spectrum of vacuum-treated sample C#1 showed a reduction in non-polar C-C/C-H components on the surface, with a ratio slightly above that of the reference sample (C#Ref), which correlates with the measured SCAs (Figure 10e). The petrol-treated sample C#2 still showed an overall average 88%increase in non-polar components, which also correlates with the measured hydrophobic wettability (Figure 10f). Broken down to the various structure types, the dimple structures of C#2 performed best, with a high 138%increase in C-C/C-H after 48 h of immersion in acetone and a superhydrophobic SCA of 153°. The immersion of samples C#3 and C#4 in 85% ethylene glycol + 15% water for 48 h resulted in a similar increase in the Fe/C ratio for acetone immersion compared to the pristine treated samples. LIPSS structures showed the highest total carbon content after glycol immersion and a high reduction in the Fe/C ratio of 65% (C#3) and 77% (C#4). C1s spectrum revealed a decrease in non-polar components for the vacuum-treated sample C#3 to 32% above the untreated reference sample C#Ref (Figure 10f). For petrol-treated sample C#4, the results also showed a reduction of non-polar components, albeit at a higher level of 44% over the untreated reference sample, contributing to the measured hydrophobic wettability and high SCAs (Figure 10g).

These research findings have significant practical implications. They reveal a clear correlation between the total carbon content (expressed by the Fe/C ratio), the non-polar/polar carbon component ratio, and the wettability properties represented by the SCA (Figure 11). This correlation suggests that to achieve superhydrophobic wettability, the carbon content should be increased, resulting in a decreased Fe/C ratio and an increased proportion of non-polar components (resulting in an increase in the C 1s NP/P ratio). This understanding can guide the design and development of materials with specific wettability properties.

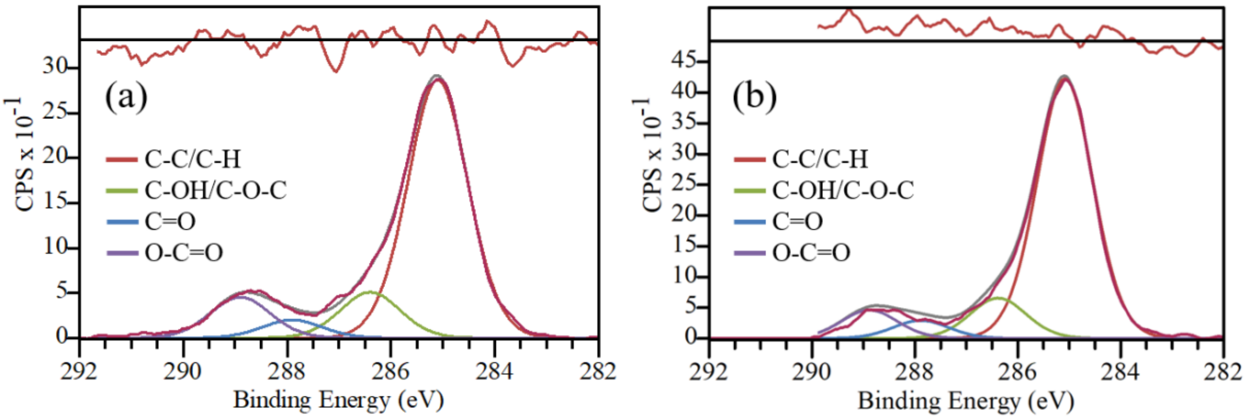

Figure 10. *Cont.*

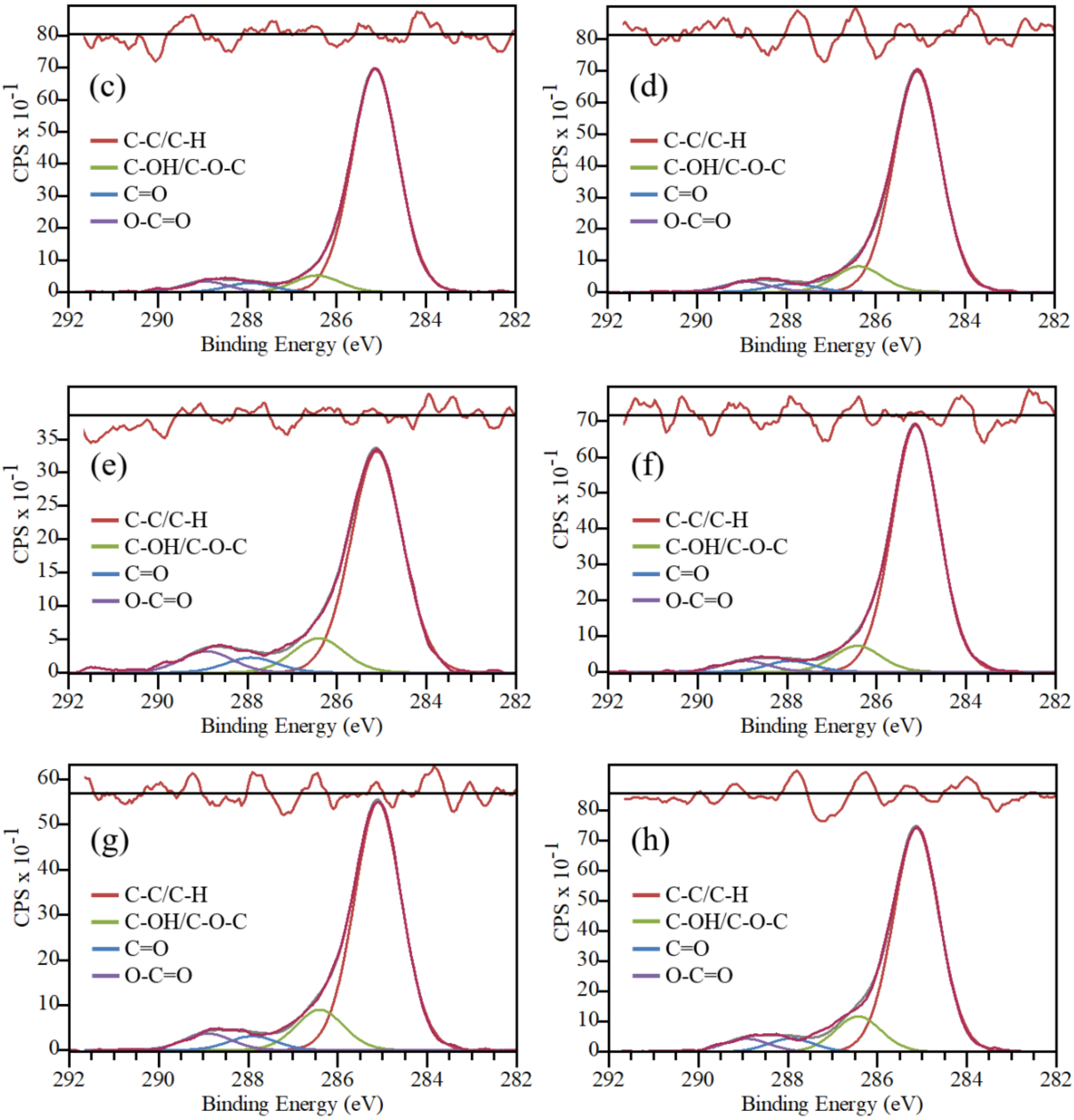

Figure 10. Deconvolution of C 1s peaks, normalized to strongest signals with residual plots on top; (**a**) unstructured, untreated reference surface; (**b**) sample C#Ref: structured (LIPSS), untreated reference surface; (**c**) sample C#RefVac: structured (LIPSS), vacuum-treated surface (4 h); (**d**) sample C#RefPet: structured (LIPSS), petrol-treated surface (4 h); (**e**) sample C#1: structured (LIPSS), vacuum-treated (4 h), corroded (48 h, acetone) surface; (**f**) sample C#2: structured (LIPSS), petrol-treated (4 h), corroded (48 h, acetone) surface; (**g**) sample C#3: structured (LIPSS), vacuum-treated, corroded (48 h, ethylene glycol) surface; (**h**) sample C#4: structured (LIPSS), petrol-treated, corroded (48 h, ethylene glycol) surface.

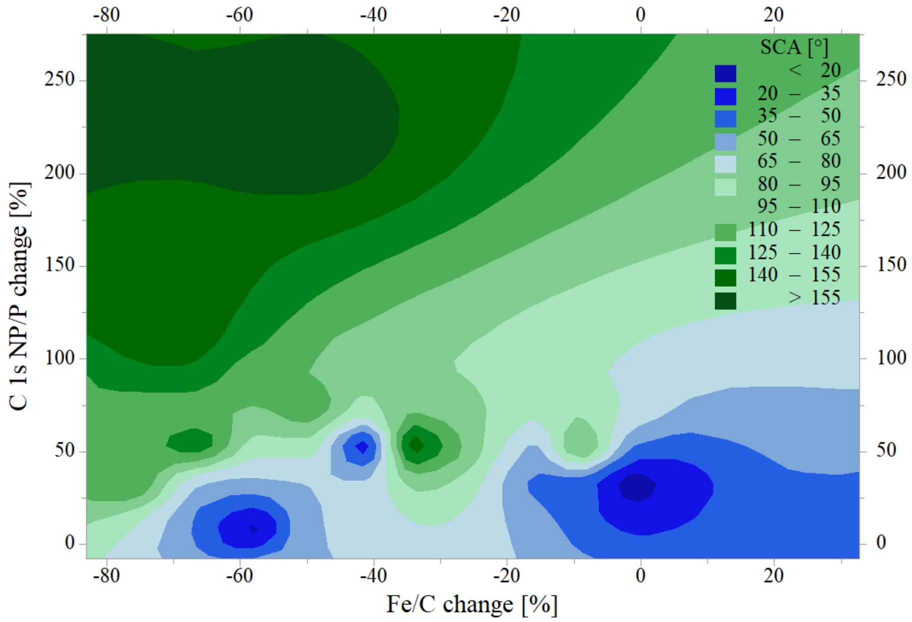

Figure 11. Contour plot of the static contact angle (SCA) versus C 1s non-polar/polar ratio and Fe/C change, including all structure types of samples C#1, C#2, C#3, C#4, C#RefVac, and C#RefPet, compared to the untreated laser-structured reference sample C#Ref (zero-reference).

The different laser-generated structures showed comparable results, pointing toward high non-polar carbon components for high SCA. The correlation between the total carbon content, non-polar/polar carbon component ratio, and ice adhesion was unclear (Figure 12). Here, a structure dependence was found, with dimple structures showing an overall high ice adhesion and all others showing the same trend as described above for the wetting properties (Figure 13).

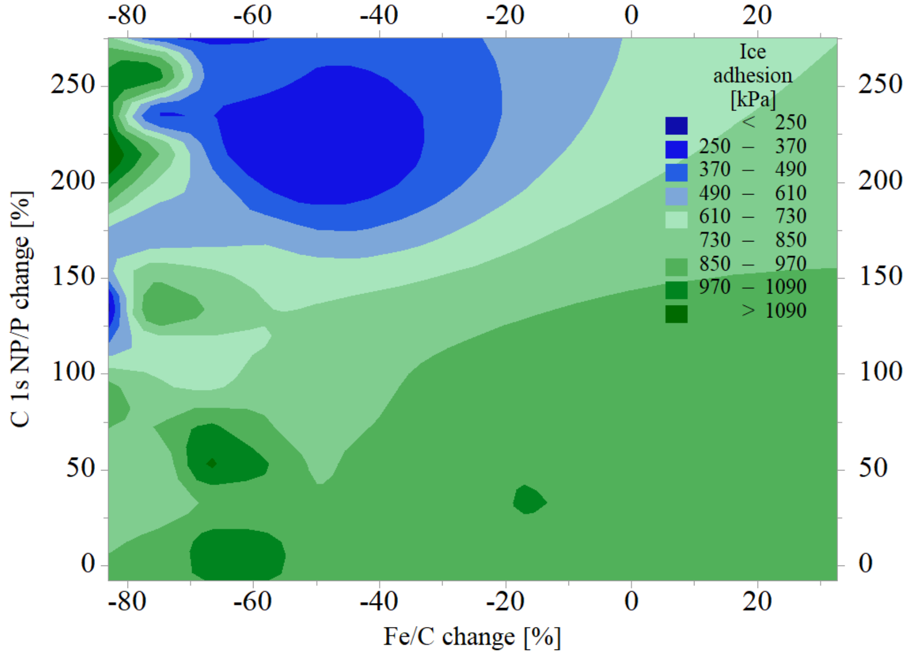

Figure 12. Contour plot of the ice adhesion versus C 1s non-polar/polar ratio and Fe/C change, including all structure types of samples C#1, C#2, C#3, C#4, C#RefVac, and C#RefPet, compared to the untreated laser-structured reference sample C#Ref (zero-reference).

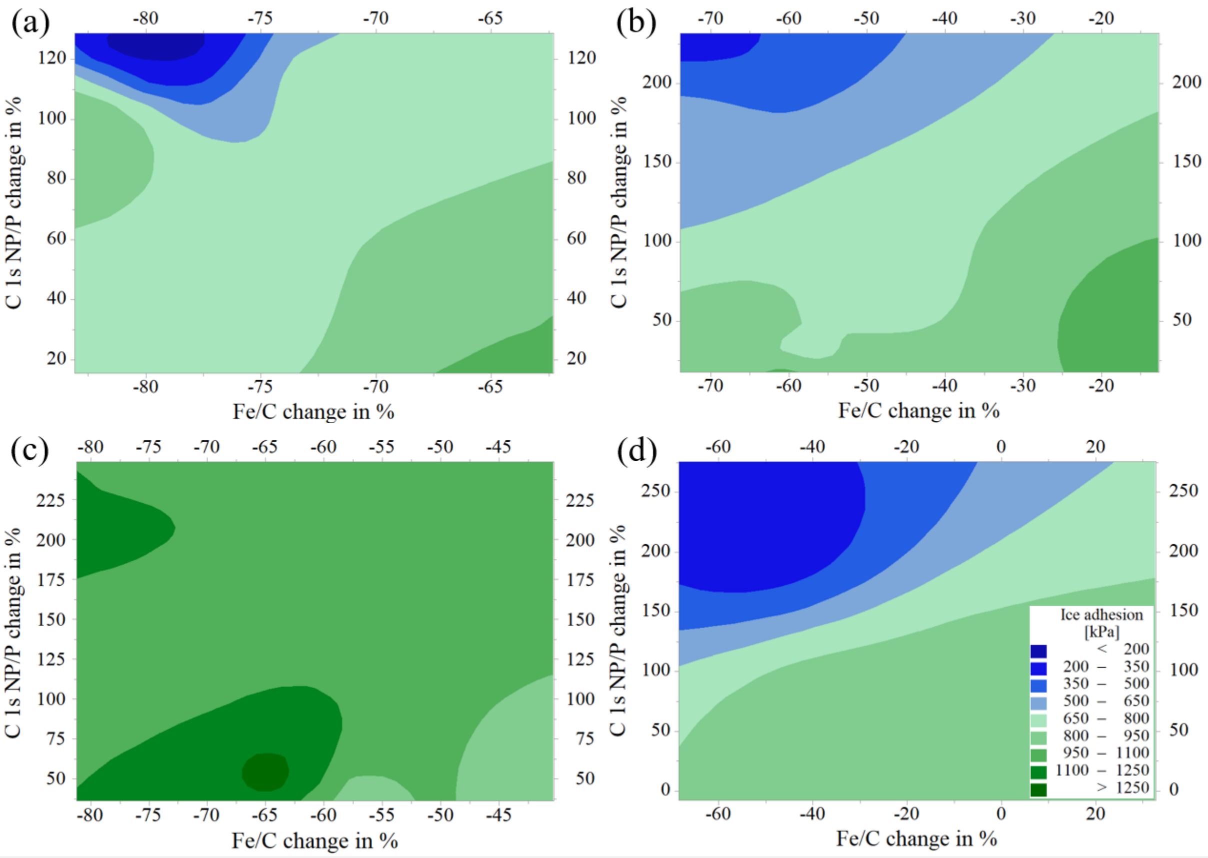

Figure 13. Contour plots of the ice adhesion versus C 1s non-polar/polar ratio and Fe/C change for (**a**) LIPSS, (**b**) grid, (**c**) dimple, and (**d**) triangle structure including samples C#1, C#2, C#3, C#4, C#RefVac, and C#RefPet, compared to the untreated laser-structured reference sample C#Ref (zero-reference).

After 48 h of acetone and ethylene glycol immersion, the vacuum-treated samples showed wettability properties and ice adhesion levels in the range of the untreated reference sample, even though the carbon content was still above the initial state. What seems to be essential for hydrophobicity is the amount of non-polar components on the surface–in the case of sample C#1, a high carbon content was found, but fewer non-polar C-C/C-H components than on sample C#2, which also showed more overall carbon (Table 4). Interestingly, in terms of non-polar/polar change, the results did not reveal much difference between samples C#3 and C#4, even though the mean SCA showed a large gap, reaching from 44° for C#3 to 139° for C#4. This explanation could again be linked to the total carbon content, which was significantly higher for C#4, with a mean Fe/C change of −58% compared to −21% for C#3. Combined with the more significant non-polar component portion of sample C#4 (44% to 32% for C#3), it could be assumed that more C-C/C-H was left. Considering these results, the petrol-treated samples showed better resistance to the tested liquids than the vacuum-treated samples. This could be linked to stronger chemisorption of hydrocarbons via immersion in petrol or the formation of a thicker hydrocarbon layer.

3.5. Optical Durability (UV)

Samples C#5 and C#6 were exposed to UV radiation for 100 h—SCA and ice adhesion were measured before and after exposure for both treatments. The results showed a sharp decrease in SCA for all structure types, except LIPSS (Table 6). It was found that the samples treated with petrol showed significant SCA degradation compared to the vacuum-treated samples for the grid, dimple, and triangle structures. LIPSS, on the other hand, largely retained their hydrophobic wetting behavior, exhibiting only a minor decrease in SCA. However, the results of the ice adhesion measurements indicated a different picture—according to these, all structures investigated showed a significant increase in ice adhesion and again reached a level comparable to that of the untreated, laser-structured sample (C#Ref).

Table 6. Results of the optical durability tests before and after exposure, IA—ice adhesion.

Sample ID	Structure Type	Treatment Method	Initial		After 100 h UV Exposure		Change	
			SCA [°]	IA [kPa]	SCA [°]	IA [kPa]	SCA	IA
C#5	LIPSS	4 h vacuum	152	179	147	648	−3%	263%
	Grid		158	337	49	867	−69%	157%
	Dimple		159	1147	121	945	−24%	−18%
	Triangle		155	292	63	926	−59%	217%
C#6	LIPSS	4 h petrol	144	661	126	772	−13%	17%
	Grid		163	535	0	907	−100%	69%
	Dimple		166	1566	6	823	−96%	−47%
	Triangle		163	309	12	895	−93%	190%

3.6. Summary

Based on the presented results, it is not possible to make a general assessment of the practical suitability of the tested surfaces. This is due to the necessity of carefully choosing chemical resistance tests, as different conditions exist in each application [63]. In this work, the main focus was on applications in aviation and wind energy. In none of these areas is the contact of the surfaces with acetone realistic, but this extreme case should still be examined during this study. Surface contact with ethylene glycol is more realistic and may impact commercial aviation applications, such as leading edge modification. The results indicate a limitation in chemical durability against de-icing liquid; however, due to the reduced ice adhesion, different ground de-icing methods without chemical deicers could be applied, e.g., a combination of surface modification and efficient electrical heating [64].

The very thin hydrocarbon layer formed during post-laser treatments resulted in low UV durability of the modified surfaces. This is a significant finding, as it suggests that the photodegradation of hydrocarbons under UV exposure [65] limits the outdoor use of the modified surfaces. However, it is important to note that accelerated UV exposure tests cannot be directly applied to real-world scenarios, and further investigation is necessary to fully understand the implications of this result.

Overall, LIPSS showed the highest contact angle after the chemical and UV durability tests, which is due to the influence of the surface topography and is consistent with previous results [33]. In terms of ice adhesion, the results of the LIPSS were no better than those of the other structure types.

4. Conclusions

The chemical and optical durability of hydrophobic/icephobic hydrocarbon layers on femtosecond laser-structured stainless steel surfaces formed during hydrocarbon/vacuum treatment was investigated. The LIPSS nanostructures and hierarchical grid, dimple, and triangle microstructures were compared to evaluate the effect of the structure type on the chemical resistance. XPS analysis showed that the static water contact angle strongly depends on the absolute amount of non-polar C-C/C-H components on the surface, which underwent reduction during all durability tests. Ice adhesion measurements revealed improved initial de-icing properties for structures with low roughness (LIPSS, grid, and triangle).

The main conclusions of this work are as follows:

- Increasing the non-polar carbon components on the laser-structured surface leads to a higher static contact angle and lower ice adhesion. This can be achieved by petrol immersion or vacuum treatment.
- The overall carbon content increases with increasing accumulated laser fluence for direct laser-ablated structure types, excluding LIPSS, where the carbon content increased despite the low accumulated laser fluence used.
- The contact angle hysteresis does not directly correlate with the icephobic properties.
- The chemical resistance depends mainly on the type of post-laser treatment and only to a limited extent on the applied structure type.
- Vacuum-treated laser-structured stainless steel surfaces are not permanently durable against ethylene glycol or acetone. They lose their superhydrophobic properties and show increased ice adhesion after 1 h of immersion.
- Re-exposure to vacuum after immersion in acetone can recover the hydrophobic wettability of those surfaces and partially their icephobic properties.
- Petrol-treated laser-structured stainless steel surfaces retain their hydrophobic properties with only minor deterioration after 48 h of immersion in ethylene glycol or acetone, although the ice adhesion increases significantly.
- None of the investigated surfaces are long-term resistant to UV irradiation, although LIPSS nanostructures maintain a hydrophobic wettability after 100 h of exposure.
- LIPSS combined with petrol treatment showed the best results in terms of hydrophobicity, lowered ice adhesion, and durability.

Supplementary Materials: The following supporting information can be downloaded at: https://www.mdpi.com/article/10.3390/coatings14080924/s1, Table S1: Experimental results of the contact angle and ice adhesion measurements using distilled water as test liquid (SD–standard deviation); Table S2: Experimental results of the XPS analysis.

Author Contributions: Conceptualization, R.F. and G.L.; methodology, R.F. and G.G.; software, R.F. and G.G.; validation, R.F. and G.L.; formal analysis, G.L. and R.F.; investigation, R.F. and G.G.; resources, G.L. and A.O.; data curation, R.F., G.G. and G.L.; writing—original draft preparation, R.F. and G.G.; writing—review and editing, R.F., G.L. and A.O.; visualization, R.F. and G.G.; supervision, G.L. and A.O.; project administration, G.L. and R.F.; funding acquisition, G.L., R.F. and A.O. All authors have read and agreed to the published version of the manuscript.

Funding: This research received funding from the Austrian Research Promotion Agency FFG "Take Off" program, project number 43317863.

Institutional Review Board Statement: Not applicable.

Informed Consent Statement: Not applicable.

Data Availability Statement: The original contributions presented in the study are included in the article/supplementary material, further inquiries can be directed to the corresponding author.

Acknowledgments: The authors acknowledge the Analytical Instrumentation Center (TU Wien) and especially Markus Sauer for their contribution to XPS analysis.

Conflicts of Interest: The authors declare no conflicts of interest.

References

1. Hudecz, A.; Koss, H.; Hansen, M.O.L. Ice accretion on wind turbine blades. In Proceedings of the 15th International Workshop Atmospheric Icing of Structures (IWAIS XV), St. John's, NL, Canada, 8–13 September 2013.
2. Parent, O.; Ilinca, A. Anti-icing and de-icing techniques for wind turbines: Critical review. *Cold Reg. Sci. Technol.* **2011**, *65*, 88–96. [CrossRef]
3. Seifert, H.; Wsterhellweg, A.; Kröning, J. Risk Analysis of Ice Throw from Wind Turbines. BOREAS 6, 2003 (Conference Paper, Presented at BOREAS 6, 9 to 11 April 2003, Pyhä, Finland. Available online: https://www.researchgate.net/publication/237537084_Risk_Analysis_of_Ice_Throw_from_Wind_Turbines (accessed on 15 July 2024).

4. Wang, K.; Xue, Y.; Tian, H.; Wang, M.; Wang, X. The impact of icing on the airfoil on the lift-drag characteristics and maneuverability characteristics. *Math. Probl. Eng.* **2021**, *16*, 5568740. [CrossRef]
5. Bragg, M.B.; Broeren, A.P.; Blumenthal, L.A. Iced-airfoil aerodynamics. *Prog. Aerosp. Sci.* **2005**, *41*, 323–362. [CrossRef]
6. Hasager, C.B.; Vejen, F.; Skrzypiński, W.R.; Tilg, A.-M. Rain erosion load and its effect on leading-edge lifetime and potential of erosion-safe mode at wind turbines in the north sea and baltic sea. *Energies* **2021**, *14*, 1959. [CrossRef]
7. Han, W.; Kim, J.; Kim, B. Study on correlation between wind turbine performance and ice accretion along a blade tip airfoil using CFD. *J. Renew. Sustain. Energy* **2018**, *10*, 023306. [CrossRef]
8. Kyle, R.; Wang, F.; Forbes, B. The effect of a leading edge erosion shield on the aerodynamic performance of a wind turbine blade. *Wind. Energy* **2019**, *23*, 953–966. [CrossRef]
9. Maissan, J.F. Wind power development in sub-arctic conditions with severe rime icing. In Proceedings of the Circumpolar Climate Change Summit and Exposition, TSYE Corporation: Circumpolar Climate Change Summit, Whitehorse, YT, Canada, 19–21 March 2001.
10. Battisti, L.; Fedrizzi, R.; Brighenti, A.; Laakso, T. Sea ice and icing risk for offshore wind turbines. In Proceedings of the OWEMES, Citavecchia, Italy, 20–22 April 2006; pp. 20–22.
11. Fakorede, O.; Feger, Z.; Ibrahim, H.; Ilinca, A.; Perron, J.; Masson, C. Ice protection systems for wind turbines in cold climate: Characteristics, comparisons and analysis. *Renew. Sustain. Energy Rev.* **2016**, *65*, 662–675. [CrossRef]
12. Huang, X.; Tepylo, N.; Pommier-Budinger, V.; Budinger, M.; Bonaccurso, E.; Villedieu, P.; Bennani, L. A survey of icephobic coatings and their potential use in a hybrid coating/active ice protection system for aerospace applications. *Prog. Aerosp. Sci.* **2019**, *105*, 74–97. [CrossRef]
13. Yadav, B. Design and analysis of a new type of aircraft wing leading edge against bird-impact. *J. Eng. Sci.* **2017**, *6*, 23–47.
14. Airbus, S.A.S. *Single Aisle, Technical Training Manual, Maintenance Course—T1, Structure*; Blagnac, France, 2005.
15. Özen, I.; Gedikli, H.; Öztürk, B. Improvement of solid particle erosion resistance of helicopter rotor blade with hybrid composite shield. *Eng. Fail. Anal.* **2021**, *121*, 105175. [CrossRef]
16. Edwards, K.L.; Davenport, C. Materials for rotationally dynamic components: Rationale for higher performance rotor-blade design. *Mater. Des.* **2006**, *27*, 31–35. [CrossRef]
17. *SAE Standard AS6285E*; SAE International Technical Standard, Aircraft Ground Deicing/Anti-Icing Processes, Revised May 2023, Issued August 2016. SAE International: Warrendale, PA, USA, 2023. [CrossRef]
18. *SAE Standard AMS1424/2A*; SAE International Material Specification, Deicing/Anti-Icing Fluid, Aircraft SAE Type I Non-Glycol Based, Revised December 2023, Issued May 2016. SAE International: Warrendale, PA, USA, 2023. [CrossRef]
19. *ISO Standard 11075:2007*; ISO International Standard, Aircraft—De-Icing/Anti-Icing Fluids—ISO Type I. Available online: https://www.iso.org/standard/44185.html (accessed on 15 July 2024).
20. *SAE Standard AMS1428/1A*; SAE International Material Specification, Fluid, Aircraft Deicing/Anti-Icing, Non-Newtonian (Pseudoplastic), SAE Types II, III, and IV Glycol (Conventional and Nonconventional) Based, Revised December 2023, Issued February 2017. SAE International: Warrendale, PA, USA, 2023. [CrossRef]
21. *ISO Standard 11078:2007*; ISO International Standard, Aircraft—De-Icing/Anti-Icing Fluids—ISO Types II, III, IV. Available online: https://www.iso.org/standard/44186.html (accessed on 15 July 2024).
22. Bowman, G.; Corsi, S.R.; Ferguson, L.; Geis, S.W.; Gold, H.; Joback, H.; Mericas, D. *Alternative Aircraft and Pavement Deicers and Anti-Icing Formulations with Improved Environmental Characteristics*; Transportation Research Board: Washington, DC, USA, 2010. [CrossRef]
23. Ferrari, M.; Cirisano, F. Superhydrophobic coating solutions for deicing control in aircraft. *Appl. Sci.* **2023**, *13*, 11684. [CrossRef]
24. Hu, H.; Liu, Y.; Gao, L. *Wind Turbine Icing Physics and Anti-/De-Icing Technology*; Elsevier: Amsterdam, The Netherlands, 2022; ISBN 978-0-12-824532-3.
25. Volpe, A.; Gaudiuso, C.; Ancona, A. Laser fabrication of anti-icing surfaces: A review. *Materials* **2020**, *13*, 5692. [CrossRef]
26. Lytvynenko, I.V.; Maruschak, P.O. Analysis of the state of the modified nanotitanium surface with the use of the mathematical model of a cyclic random process. *Optoelectron. Instrument. Proc.* **2015**, *51*, 254–263. [CrossRef]
27. Hutsaylyuk, V.; Lytvynenko, I.; Maruschak, P.; Dzyura, V.; Schnell, G.; Seitz, H. A new method for modeling the cyclic structure of the surface microrelief of titanium alloy Ti6Al4V after processing with femtosecond pulses. *Materials* **2020**, *13*, 4983. [CrossRef]
28. Sataeva, N.E.; Boinovich, L.B.; Emelyanenko, K.A.; Domantovsky, A.G.; Emelyanenko, A.M. Laser-assisted processing of aluminum alloy for the fabrication of superhydrophobic coatings withstanding multiple degradation factors. *Surf. Coat. Technol.* **2020**, *397*, 125993. [CrossRef]
29. Memon, H.; Wang, J.; Hou, X. Interdependence of surface roughness on icephobic performance: A review. *Materials* **2023**, *16*, 4607. [CrossRef]
30. Fortin, G.; Perron, J. Ice adhesion models to predict shear stress at shedding. *J. Adhes. Sci. Technol.* **2012**, *26*, 523–553. [CrossRef]
31. Jung, Y.S.; Baeder, J. Simulations for effect of surface roughness on wind turbine aerodynamic performance. *J. Phys. Conf. Ser.* **2020**, *1452*, 012055. [CrossRef]
32. Vercillo, V.; Tonnicchia, S.; Romano, J.-M.; García-Girón, A.; Aguilar-Morales, A.I.; Alamri, S.; Dimov, S.S.; Kunze, T.; Lasagni, A.F.; Bonaccurso, E. Design rules for laser-treated icephobic metallic surfaces for aeronautic applications. *Adv. Funct. Mater.* **2020**, *30*, 1910268. [CrossRef]

33. Fürbacher, R.; Liedl, G. Investigations on the wetting and deicing behavior of laser treated hydrophobic steel surfaces. In Proceedings of the Laser-Based Micro- and Nanoprocessing XV, Online, 6–11 March 2021. [CrossRef]
34. Fürbacher, R.; Liedl, G.; Otto, A. Fast transition from hydrophilic to superhydrophobic, icephobic properties of stainless steel samples after femtosecond laser processing and exposure to hydrocarbons. *Procedia CIRP* **2022**, *111*, 643–647. [CrossRef]
35. Fürbacher, R.; Liedl, G.; Grünsteidl, G.; Otto, A. Icing wind tunnel and erosion field tests of superhydrophobic surfaces caused by femtosecond laser processing. *Wind* **2024**, *4*, 155–171. [CrossRef]
36. Bouchard, F.; Soldera, M.; Baumann, R.; Lasagni, A.F. Hierarchical microtextures embossed on PET from laser-patterned stamps. *Materials* **2021**, *14*, 1756. [CrossRef]
37. Velten, T.; Bauerfeld, F.; Schuck, H.; Scherbaum, S.; Landesberger, C.; Bock, K. Roll-to-roll hot embossing of microstructures. *Microsyst. Technol.* **2010**, *17*, 619–627. [CrossRef]
38. Xu, J.; Su, Q.; Shan, D.; Guo, B. Sustainable micro-manufacturing of superhydrophobic surface on ultrafine-grained pure aluminum substrate combining micro-embossing and surface modification. *J. Clean. Prod.* **2019**, *232*, 705–712. [CrossRef]
39. Fu, Y.; Soldera, M.; Wang, M.; Milles, S.; Deng, K.; Voisiat, B.; Nielsch, K.; Lasagni, A.F. Wettability control of polymeric microstructures replicated from laser-patterned stamps. *Sci. Rep.* **2020**, *10*, 22428. [CrossRef]
40. Yeong, Y.H.; Gupta, M.C. Hot embossed micro-textured thin superhydrophobic Teflon FEP sheets for low ice adhesion. *Surf. Coat. Technol.* **2017**, *313*, 17–23. [CrossRef]
41. Kulinich, S.A.; Farzaneh, M. How wetting hysteresis influences ice adhesion strength on superhydrophobic surfaces. *Langmuir* **2009**, *25*, 8854–8856. [CrossRef]
42. Kulinich, S.A.; Farzaneh, M. Ice adhesion on super-hydrophobic surfaces. *Appl. Surf. Sci.* **2009**, *255*, 8153–8157. [CrossRef]
43. Janjua, Z.A.; Turnbull, B.; Choy, K.-L.; Pandis, C.; Liu, J.; Hou, X.; Choi, K.-S. Performance and durability tests of smart icephobic coatings to reduce ice adhesion. *Appl. Surf. Sci.* **2017**, *407*, 555–564. [CrossRef]
44. Momen, G.; Jafari, R.; Farzaneh, M. Ice repellency behaviour of superhydrophobic surfaces: Effects of atmospheric icing conditions and surface roughness. *Appl. Surf. Sci.* **2015**, *349*, 211–218. [CrossRef]
45. Choi, W.; Tuteja, A.; Mabry, J.M.; Cohen, R.E.; McKinley, G.H. A modified Cassie–Baxter relationship to explain contact angle hysteresis and anisotropy on non-wetting textured surfaces. *J. Colloid Interface Sci.* **2009**, *339*, 208–216. [CrossRef]
46. Yang, C.; Chao, J.; Zhang, J.; Zhang, Z.; Liu, X.; Tian, Y.; Zhang, D.; Chen, F. Functionalized CFRP surface with water-repellence, self-cleaning and anti-icing properties. *Coll. Surf. A Physicochem. Eng. Asp.* **2020**, *586*, 124278. [CrossRef]
47. Cardoso, J.T.; Garcia-Girón, A.; Romano, J.M.; Huerta-Murillo, D.; Jagdheesh, R.; Walker, M.; Dimov, S.S.; Ocaña, J.L. Influence of ambient conditions on the evolution of wettability properties of an IR-, ns-laser textured aluminium alloy. *RSC Adv.* **2017**, *7*, 39617–39627. [CrossRef]
48. Yang, Z.; Liu, X.; Tian, Y. Insights into the wettability transition of nanosecond laser ablated surface under ambient air exposure. *Adv. Colloid Interface Sci.* **2019**, *533*, 268–277. [CrossRef]
49. Korhonen, J.T.; Huhtamäki, T.; Ikkala, O.; Ras, R.H.A. Reliable measurement of the receding contact angle. *Langmuir* **2013**, *29*, 3858–3863. [CrossRef]
50. Meuler, A.J.; Smith, J.D.; Varanasi, K.K.; Mabry, J.M.; McKinley, G.H.; Cohen, R.E. Relationships between Water Wettability and Ice Adhesion. *ASC Appl. Mater. Interfaces* **2010**, *2*, 3100–3110. [CrossRef]
51. Wang, C.; Zhang, W.; Siva, A.; Tiea, D.; Wynne, K.J. Laboratory test for ice adhesion strength using commercial instrumentation. *Langmuir* **2014**, *30*, 540–547. [CrossRef]
52. Goraj, Z. An overview of the deicing and antiicing technologies with respects for the future. In Proceedings of the 24th International Congress of the Aeronautical Sciences, Yokohama, Japan, 29 August–3 September 2004.
53. FAA Holdover Time Guidelines, Winter 2023–2024, Issued in August 2023. Available online: https://www.faa.gov/other_visit/aviation_industry/airline_operators/airline_safety/deicing (accessed on 15 July 2024).
54. *ASTM Standard D7869-17*; ASTM International Standard, Standard Practice for Xenon Arc Exposure Test with Enhanced Light and Water Exposure for Transportation Coatings. Available online: https://www.astm.org/d7869-17.html (accessed on 15 July 2024).
55. IEC Technical Specification, Measurement Procedures for Materials Used in Photovoltaic Modules—Part 7-2: Environmental Exposures—Accelerated Weathering Tests of Polymeric Materials, IEC Technical Specification IEC TS 62788-7-2:2017. Available online: https://webstore.iec.ch/en/publication/33675 (accessed on 15 July 2024).
56. Gurevich, E.L.; Gurevich, S.V. Laser induced periodic surface structures induced by surface plasmons coupled via roughness. *Appl. Surf. Sci.* **2014**, *302*, 118–123. [CrossRef]
57. Otto, A. Excitation of nonradiative surface plasma waves in silver by the method of frustrated total reflection. *Phys. A Hadron. Nucl.* **1968**, *216*, 398–410. [CrossRef]
58. Zhou, K.; Jia, X.; Jia, T.; Cheng, K.; Cao, K.; Zhang, S.; Feng, D.; Sun, Z. The influences of surface plasmons and thermal effects on femtosecond laser-induced subwavelength periodic ripples on Au film by pump-probe imaging. *J. Appl. Phys.* **2017**, *121*, 104301. [CrossRef]
59. Fuerbacher, R.; Liedl, G.; Murzin, S. Experimental study of spatial frequency transition of laser induced periodic surface structures. *J. Phys. Conf. Ser.* **2021**, *1745*, 012017. [CrossRef]
60. Milne, A.J.B.; Amirfazli, A. The Cassie equation: How it is meant to be used. *Adv. Colloid Interface Sci.* **2012**, *170*, 48–55. [CrossRef]

61. Hauschwitz, P.; Jagdheesh, R.; Rostohar, D.; Brajer, J.; Kopeček, J.; Jiřícek, P.; Houdková, J.; Mocek, T. Hydrophilic to ultrahydrophobic transition of Al 7075 by affordable ns fiber laser and vacuum processing. *Appl. Surf. Sci.* **2020**, *505*, 144523. [CrossRef]
62. Jagdheesh, R.; Pathiraj, B.; Karatay, E.; Römer, G.R.B.E.; in't Veld, A.J.H. Laser-induced nanoscale superhydrophobic structures on metal surfaces. *Langmuir* **2011**, *27*, 8464–8469. [CrossRef]
63. Nistal, A.; Sierra-Martin, B.; Fernandez-Barbero, A. On the durability of icephobic coatings: A review. *Materials* **2024**, *17*, 235. [CrossRef]
64. Zhao, Z.; Chen, H.; Liu, X.; Liu, H.; Zhang, D. Development of high-efficient synthetic electric heating coating for anti-ice/de-icing. *J. Surf. Coat. Technol.* **2018**, *349*, 340–346. [CrossRef]
65. Janus, R.; Kolomanski, K.; Wadrzyk, M.; Lewandowski, M. Degradation of petroleum diesel fuel accelerated by UV irradiation: The impact of ageing on chemical composition and selected physicochemical properties. *E3S Web. Conf.* **2019**, *108*, 02003. [CrossRef]